Underlying Mechanisms of Reactive Oxygen Species and Oxidative Stress photoinduced by Graphene and its Surface Functionalized Derivatives

Journal:	*Environmental Science: Nano*
Manuscript ID	EN-ART-11-2019-001295.R1
Article Type:	Paper

Environmental significance

Toxicity of graphene and its surface functionalized derivatives is closely relevant to their ability of reactive oxygen species (ROS) production. Understanding the mechanisms of ROS generation induced by graphene materials is valuable for evaluating their toxicity and potential environmental risks. This study determined the photogenerated ROS and oxidative stress induced by graphene nanomaterials. The photochemical pathways of ROS production were identified by conducting density functional theory (DFT) calculation. By comparing the biological redox potential and the lowest occupied molecular orbital values of the substances, u-G and G-COOH were predicted to have the potential of inducing oxidative stress. This prediction was validated in *Daphnia magna* by detecting the levels of oxidative stress biomarkers. By coupling experimental observations with the theoretically predictions, the predictive toxicological paradigm provides mechanistic insight to understand the photochemical activity and toxicity of graphene nanomaterials. It is of considerable significance for regulatory decision-making about carbon nanomaterials.

Underlying Mechanisms of Reactive Oxygen Species and Oxidative Stress photoinduced by Graphene and its Surface Functionalized Derivatives

Hongye Yao[a,#], Yang Huang[a,#], Xuan Li[a,#], Xuehua Li[a,*], Hongbin Xie[a], Tianlie Luo[a], Jingwen Chen[a], Zhongfang Chen[b]

[a]Key Laboratory of Industrial Ecology and Environmental Engineering (MOE), School of Environmental Science and Technology, Dalian University of Technology, Linggong Road 2, Dalian 116024, China.

[b]Department of Chemistry, University of Puerto Rico, San Juan, Puerto Rico 00931, United States.

[#] These authors contributed equally to the paper.

[*] Corresponding author: 0411-84707844, E-mail: lixuehua@dlut.edu.cn

ABSTRACT: Graphene can be modified by different functional groups through various transformation processes in the environment. Toxicological activity of graphene is closely relevant to its ability of reactive oxygen species (ROS) production, which can be altered by the surface modification. Herein, unfunctionalized graphene (u-G), carboxylated graphene (G-COOH) and aminated graphene (G-NH_2) were selected to determine their ability of photogenerating ROS in aqueous phase. Oxidative stress (ROS concentration and superoxide dismutase activity) in *Daphnia magna* under the simulated sunlight radiation induced by the materials were also investigated. Based on density functional theory (DFT) calculation, the photochemical pathways of ROS production were identified. G-COOH and G-NH_2 produced singlet oxygen in aqueous phase by mediating energy transfer. G-COOH, G-NH_2 and u-G generated superoxide anion and further produced hydroxyl radicals by inducing electron transfer. By comparing the biological redox potential and the lowest occupied molecular orbitals values (E_{LUMO}) of the substances, u-G and G-COOH were identified to have the potential of inducing oxidative stress. The predictive result was validated by the significant increase of oxidative stress biomarkers in *Daphnia magna*. By coupling experimental observations with the theoretically predictions, the present results provide mechanistic insight to understand the photochemical activity and toxicity of graphene and its surface functionalized derivatives.

Keywords: graphene, surface functionalization, reactive oxygen species, oxidative stress, *Daphnia magna*, Density Functional Theory (DFT)

1. Introduction

Among the numerous unique properties of carbon nanomaterials, their ability of photogenerating reactive oxygen species (ROS) has raised increasing interest in the fields of biomedicine and environmental engineering[1-2]. The application of carbon nanomaterials has increased their release into the environment, where they may pose the potential hazardous to ecological systems[3-4]. Previous studies reported that oxidative stress induced by ROS generation is one of the responsible mechanisms for the toxic effect of carbon nanomaterials[5]. Different kinds of ROS including superoxide anion ($O_2^{\bullet-}$), hydroxyl radical (•OH) and singlet oxygen ($^1O_2$)[7] result in different toxic effects. •OH is a strong and nonselective oxidant that can damage organic biomolecules, including lipids, proteins, DNA. $^1O_2$ is the main mediator of photocytoxicity and can irreversibly damage the treated tissues, causing biomembrane oxidation and degradation[8-10]. Although $O_2^{\bullet-}$ is not a strong oxidant, as a precursor for •OH and $^1O_2$, $O_2^{\bullet-}$also has significant biological implications. To evaluate their industrial applications and toxic effects, it is important to reveal the pathways of ROS production by carbon nanomaterials.

As an important branch of carbon nanomaterials, graphene can be modified by functional groups (e.g., -COOH, $-NH_2$) through a series of transformation processes after being released into the environment[11]. The surface functional groups of carbon nanomaterials may affect the types and levels of the ROS production. Indeed, both fullerene and fullerenol suspensions could transfer electron to produce $O_2^{\bullet-}$ under irradiation, but fullerenol showed a significant higher production efficiency of $O_2^{\bullet-}$ than fullerene[12]. The steady state concentration of $^1O_2$ induced by carboxylated single-walled carbon nanotubes (SWNT-COOH) was higher than that by SWNT with polyethylene glycol functionalized (SWNT-PEG), but the steady state concentration of •OH induced by SWNT-COOH was less than that by SWNT-PEG[13]. Recent study demonstrated that graphene oxide has the ability to generate $O_2^{\bullet-}$ under UV-A, but has no ability to generate •OH and $^1O_2$ under the same condition[14]. However, the influence of different kinds of surface functional groups (e.g., -COOH, -NH_2) on the ROS generation are not fully revealed for graphene nanomaterials.

Previous studies have explored a possible explanation of how specific kinds of ROS can be generated from irradiated metal oxide nanoparticle in aqueous phase by using the band energy levels[17,18]. In addition, Nel et al. found that the overlap of conduction band energy levels with the biological redox potential (-4.12 to -4.84 eV) was strongly correlated to the ability of selected metal oxide nanoparticles to induce the ROS production and oxidative stress[19]. To our knowledge, the approach based on band energy levels has not been utilized to illuminate the ROS generation and oxidative stress for graphene nanomaterials.

In this study, we performed a combined theoretical calculation and experimental study to explore the levels and pathways of ROS generation in aqueous phase and oxidative stress in *Daphnia magna* photoinduced by three representative graphene nanomaterials, i.e., unfunctionalized graphene (u-G), carboxylated graphene (G-COOH), and aminated graphene (G-NH_2). The types and levels of photoinduced ROS were determined using Electron Paramagnetic Resonance (EPR) spectroscopy and molecular probes methods, respectively. Based on density functional theory (DFT) to calculate energy of frontier molecular orbitals (the highest occupied molecular orbitals values (E_{HOMO}) and the lowest occupied molecular orbitals values (E_{LUMO})), the photochemical pathways of ROS production were identified. The experimentally measured ROS level and activity of superoxide dismutase (SOD) in *Daphnia magna* confirmed that oxidative stress potential at whole animal levels can be predicted by comparing E_{LUMO} of graphene nanomaterials with the biological redox potential (-4.12 to -4.84 eV).

2. Materials and methods

2.1 Materials. G-COOH, G-NH_2 and u-G were purchased from Nanjing XFNANO Materials Technology Company (China). The ratio of O/C in G-COOH and the ratio of N/C in G-NH_2 was 0.655 and 0.162, respectively. Furfural alcohol (FFA, 98%), 2,3-bis(2-methoxy-4-nitro-5-sulfophenyl)-2H-tetrazolium-5-carboxanilide (XTT, 90%), *p*-chlorobenzoic acid (*p*CBA, 99%), sodium dodecyl sulfate (SDS, 98%), 2,2,6,6-Tetramethylpiperidine (TEMP, 95%), 5,5-Dimethyl-1-pyrroline-N-oxide (DMPO, 90%), 2',7'-dichlorfluorescein-diacetate (DCFH-DA) and methanol were obtained from Sigma-Aldrich. Ultrapure water (>18 MΩ*cm) was purified from a Milli-Q Water Purification System (Millipore, Billerica, MA). Other reagents (purity > 99.0%) were purchased from Kermel Chemical Reagent Company (China).

2.2 Preparation of graphene suspensions and characterization. G-COOH suspension was prepared using ultrapure water by sonication under Ultrasonic cell crusher (JY92-2D, Lanzhi, China) at 400 W (intermittent ultrasound 10 s) for 2 h. Due to G-NH_2 and u-G were well dispersed at a lower SDS concentration (0.05% w/v, below the critical micelle concentration, c.m.c.), these graphene nanomaterials suspension were prepared using SDS solution (0.05% w/v). After standing the suspensions for 24 h, supernatants were collected as stock solutions and stored in brown glass bottle under dark at room temperature. A total organic carbon (TOC, Multi N/C 2100S, Analytikjena, Germany) was used to analyze stock solution concentrations.

Particle size distributions (PSDs) and zeta potentials of the G-COOH, G-NH_2 and u-G suspensions were determined by dynamic light scattering using a Malvern particle size analyzer (Nano-ZS90, Worcestershire, UK). The morphology and thickness of the particles were observed by Atomic microscope mechanics (AFM; PicoScan2500, Molecular Imaging, America). Fourier infrared spectroscopy characterization (FI-IR; EQUINOX55, Bruker, America) and Raman spectra (DRX, Therno Fisher Scientific, America) were used to analyze surface functional groups (including -COOH and $-NH_2$) and the degree of surface defects of G-COOH, G-NH_2 and u-G, respectively (Figure S1-S2). The absorption peaks of sample solutions were characterized by a UV-vis spectrophotometer (UV2900, Hitachi, Japan). The redox potential of samples was measured cyclic voltammetry (PISO-813, Taiwan).

2.3 Irradiation. The irradiation experiments in aqueous phase were performed with a Rayonet merry-go-round photochemical reactor (XPA, Xujiang, China) with quartz tubes containing the reaction solutions. A 500 W medium-pressure mercury lamp surrounded by 290 nm cut-off filters was used as the light source. The emission spectrum of mercury lamp with wavelength scanned from 290-600 nm was displayed in Figure S3a. G-COOH, G-NH_2 and u-G stock solutions were buffered to pH = 7.4 by adding appropriated phosphate buffers (e.g. KH_2PO_4, K_2HPO_4). Irradiation and control experiments were performed in triplicate and dark control were wrapped with aluminum foil. The change for functional groups and the defects degree of G-COOH, G-NH_2 and u-G after 5 h irradiation were characterized by FI-IR and Raman spectra analysis. The bioassay experiments were performed under simulated sunlight irradiation. The light source is four UV-A and four flourescent lamps. The spectrum of the simulated sunlight irradiation was provided in Figure S3b.

2.4 EPR detection of $^1O_2$ and •OH. ROS production was qualitatively determined by using Electron Paramagnetic Resonance Spectroscopy (EPR; A200, Bruker, Germany) under the following conditions: center field of 3360.00 G, microwave power of 16.77 mW, modulation frequency of 100.00 kHz, modulation amplitude of 2 G. TEMP and DMPO were used as spin-trapping agent for $^1O_2$ and •OH detection, respectively[9, 20]. Solutions containing 15 mgC/L G-COOH, G-NH_2 and u-G placed in quartz tubes were irradiated by 500 W mercury lamp with 290 nm cut-off filters for 5-20 min (i.e., not beyond 30 min to avoid the excessive degradation of TEMP[21]). After irradiation, the solutions in quartz glass tube were immediately transferred to EPR analysis. The EPR signal of TEMPO (i.e., $^1O_2$ adduct with

TEMP) and DMPO-OOH adducts (i.e., •OH adduct with DMPO) were observed to indicate the production of $^1O_2$ and •OH.

2.5 ROS measurements. The concentrations of photogenerated ROS by G-COOH, G-NH_2 and u-G suspensions were quantitatively detected by molecular probe assays. Through detecting the photodegradation rate of FFA and *p*CBA, the $^1O_2$ and •OH production were determined, respectively[22-23]. The loss concentration of FFA and *p*CBA were measured by HPLC (Agilent 1260, USA) with the UV/Vis detector set at 237 nm and 230 nm, respectively. The generation of $O_2^{\bullet-}$ was monitored by the formation of XTT-formazan at the initial concentration of 0.1 mM XTT, which was detected using a UV-vis spectrophotometer with an adsorption peak at 470 nm[6].

2.6 Model organism. *Daphnia magna* were cultured in our laboratory maintained in an artificial climate incubator with a photoperiod of 16 h and 8 h (light/dark) and a temperature of 20 ± 1°C. *Daphnia magna* were kept in glass beakers and fed with a suspension of *Chlorella pyrenoidesa* once a day. All exposure experiments were carried out in test medium ($CaCl_2$•$2H_2O$ 294 mg/L, $MgSO_4$•$7H_2O$ 23.3 mg/L, $NaHCO_3$ 64.8 mg/L, KCL 5.8 mg/L, pH 7.8±0.2 and) that was aerated for three days.

2.7 Determination of oxidative stress markers in *Daphnia magna*. DCFH-DA was used to determine the amount of ROS in *Daphnia magna*[24]. *Daphnia magna* were exposed to graphene and its surface functionalized derivatives suspensions (2 mgC/L) under dark condition for 2 h, and then irradiated for 40 min. After exposure, 3 *Daphnia magna* were transferred to a 24-well cluster plate. The remaining water was aspirated off before addition of 20 mM DCFH-DA to each well in the cluster plate. Fluorescence was measured after 5 h of dark incubation with DCFH-DA by using Microplate Reader (200 pro, Tecan Trading, Germany) at 485 and 520 nm wavelength for excitation and emission. The levels of SOD were determined using assay kits according to their instructions. Because the formation of superoxide could inhibit the transformation of hydroxylamine to nitrite, the SOD activity was measured with a spectrophotometer (UV2900, Hitachi, Japan) at 550 nm[25]. One unit of SOD was defined as the amount of enzyme required to produce a 50% inhibition in this reaction system. The activity of SOD was expressed as units per milligrams of protein (U/mg protein).

2.8 Theoretical calculation. A 28-ring structure model consisting of 78 C atoms and 24 H atoms (Table S1) was selected for simulating the graphene sheet, in which the end atoms were saturated with hydrogen atoms to reduce boundary effects[26]. The optimized C=C distances in the structure model of u-G were within the standard bond length of 1.42 Å, in excellent agreement with previously reported graphene[27]. It was also reported that carboxyl groups were mainly appeared at the edges of graphene[28-29]. Thus, carboxyl and amine groups were also considered to be on the edges of graphene in this study. According to the ratio of O/C in G-COOH and N/C in G-NH_2, the numbers of functional groups on the surface were calculated to be approximately 6 for both -COOH and -NH_2. The possible structure models of G-COOH and G-NH_2 were constructed under Material Studio 6.1 and were shown in Figure S7. Geometry optimization and frontier molecular orbital energy analysis were performed in water at the B3LYP level with the 3-21G basis set[30] using the Gaussian 09 (D.01) simulation package[30-32]. The computed $E_{\mathrm{HOMO/LUMO}}$ values of graphene using B3LYP level with the 3-21G basis set have been proven to be in excellent agreement with experimental results[30]. Integral equation form polarizable continuum model (IEFPCM) was used to simulate the solvent effect of the water[33].

2.9 Statistical analysis. Data were represented as the mean ± standard. Significant differences were determined by ANOVA with a 95% confidence interval ($p < 0.05$). Statistical analyses of data were performed using SPSS Statistics 22.0.

3. Results and discussion

3.1 Characterization of G-COOH, G-NH_2 and u-G colloidal dispersions before and after irradiation. As shown in Figure 1a, G-COOH, G-NH_2 and u-G suspensions exhibited well dispersion after 2 weeks laying at room temperature. The intensity-averaged PSDs of G-COOH, G-NH_2 and u-G dispersed in water were 383.5, 490.7 and 792.5 nm, respectively. The zeta potentials for G-COOH, G-NH_2 and u-G suspensions were -31.4, -42.1 and -37.5 mV, respectively, which implied that the suspensions had a good stability[34]. Different characteristic absorption peaks in the range 200-330 nm were found for G-COOH, G-NH_2 and u-G (Figure 1b), suggesting that mercury lamp light wavelength above 290 nm could be absorbed by the nanomaterials. AFM images of G-COOH, G-NH_2 and u-G were shown in Figure 1c, d, e, which indicated that the thicknesses of G-COOH and G-NH_2 were roughly 1.2 nm consistent with the around 1.0 nm thickness reported for single-layer graphene[35], while the thickness of u-G was roughly 2-3 nm for multi-layers distributed.

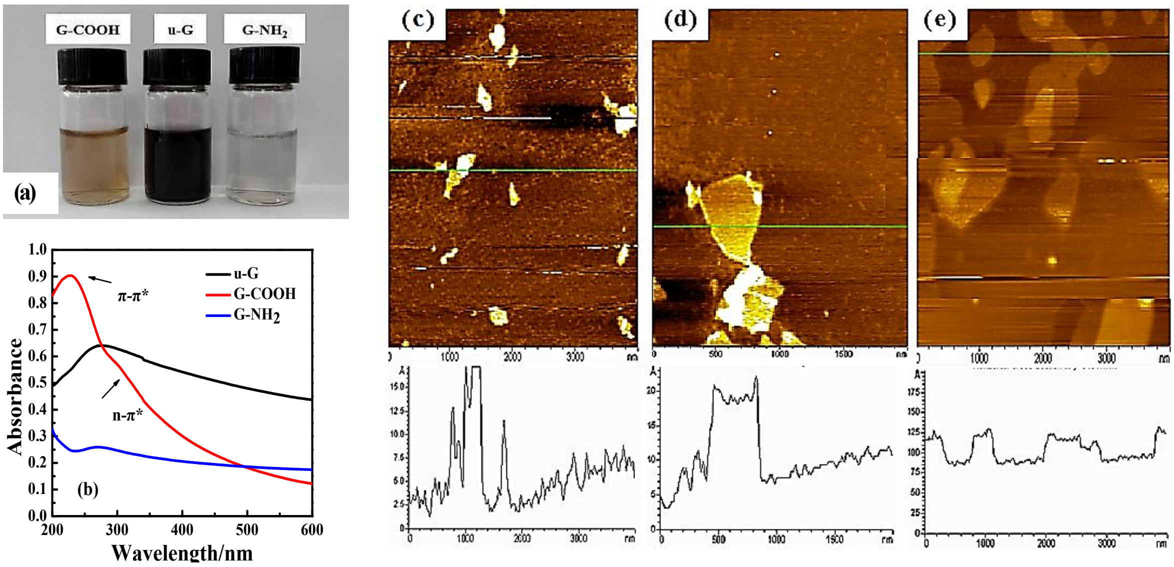

Figure 1. Characterizations of G-COOH, G-NH_2 and u-G: (a) dispersion solutions after 2 weeks laying at room temperature; (b) absorption spectrums and (c, d, e) AFM images of G-COOH, G-NH_2 and u-G.

FT-IR was used to characterize surface chemistry of G-COOH, G-NH_2 or u-G before and after 5 h irradiation (Figure S1). Before irradiation, the peaks at 3000-3400 cm^{-1} were assigned to O-H and N-H bands, which represented two kinds of surface modification groups. After 5 h treatments, there still existed O-H and N-H peaks at 3000-3400 cm^{-1}, but the peaks at 3000 cm^{-1} belong to C-H bands was appeared, which suggested that defects appeared on the surface of graphene for G-COOH and G-NH_2[12]. Moreover, the C=O peaks (1730 cm^{-1}) in the spectra of G-COOH became weaker (Figure S1b) after 5h light exposure, implying that oxygen functional groups were slightly decreased during irradiation[36].

The changes in surface structure of G-COOH, G-NH_2 and u-G after irradiation (0 h, 2 h and 6 h) were measured by Raman spectrum (Figure S2). The two distinct bands located at ~1360 and ~1580 cm^{-1} were corresponding to the D-band (defects or amorphous carbon) and G-band (well-ordered sp^2 carbon), respectively[36-37]. Hence, the intensity ratio of I_D/I_G was used to evaluate the degree of defects or functionalization. The variation ratio of I_D/I_G for G-COOH and G-NH_2 after 6 h irradiation was 6.8% and 7%, respectively. Previous studies found that the I_D/I_G variation of MWNTs-COOH was more than 30% under 48 h irradiation due to the degradation of carboxyl groups on the surface[38]. The I_D/I_G variations for G-COOH and G-NH_2 were lower than 10% during 6 h irradiation, suggesting that the change of surface functional groups were negligible under irradiation. However, the Raman spectrum of pristine graphite displayed a only prominent G peak at 1582 cm^{-1}[39], and the ratio of I_D/I_G for u-G before irradiation was 1.021, indicating that the defects existed on the surface.

3.2 EPR detection of ROS. As shown in Figure 2, there were three evident characteristic peaks of TEMPO (adduct of $^1O_2$ with TEMP) with the coexistence of TEMP with G-COOH (irradiation 0-10 min) or G-NH_2, u-G, SDS (irradiation 20 min). In the dark controls, there were no EPR signals (Figure S4). But there was no significant difference in the signal intensity of TEMPO between u-G suspensions containing SDS (0.05% w/v) and SDS solutions (0.05% w/v) under same irradiation time (Figure 2c, d). These results indicated that u-G has no ability to photogenerate $^1O_2$ and graphene modified by amino functional groups or carboxyl groups can photogenerate $^1O_2$, which the production rate of $^1O_2$ by G-COOH was much faster than that by G-NH_2. By the DFT calculations, previous study suggested that carboxyl functionalization on carbon nanotubes increased the active sites[40]. These ‘‘active sites’’ disrupted aromaticity, and increased photochemical reactivity compared to unfunctionalized nanotubes[41].

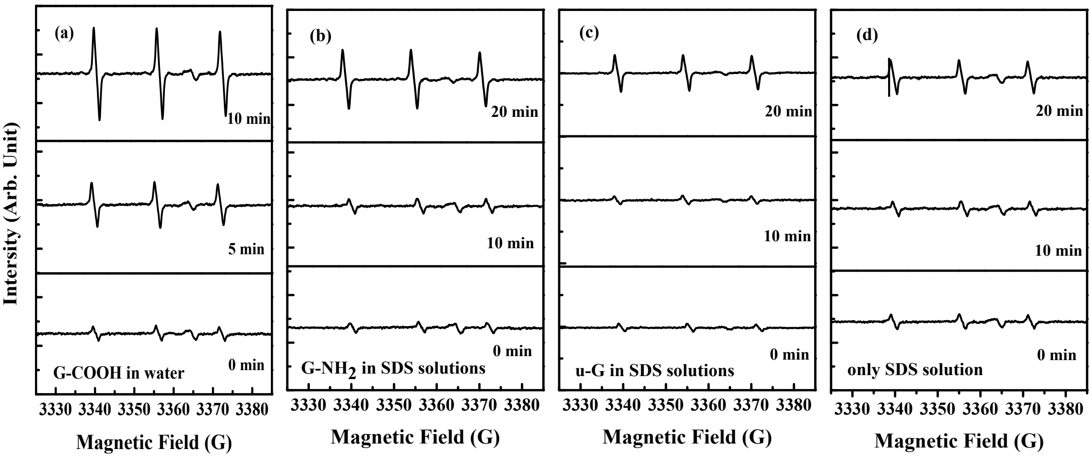

Figure 2. EPR spectrum of TEMP (50 mM) adduct with $^1O_2$ production in the G-COOH, G-NH_2 and u-G aqueous suspensions (15 mgC/L) and SDS solution (0.05% w/v).

In the case of •OH, the characteristic quartet peaks with 1:2:2:1 were observed by EPR detection of •OH spin adduct (DMPO/•OH)[42]. The characteristic peak of DMPO-OOH adducts in G-COOH, G-NH_2 and u-G suspensions were measured with or without irradiation. As the results, no significant signal of DMPO-OOH in G-COOH, G-NH_2 and u-G suspensions was observed in the dark (Figure S4), but there were obvious four characteristic peaks for •OH production under irradiation (Figure 3a, b, c). Similar to photochemical generation of $^1O_2$, the production rate of •OH by G-COOH was much faster than that by G-NH_2 and u-G. The signal of DMPO presented at 20 min irradiation in the G-NH_2 and u-G suspensions and the SDS solutions (0.05% w/v) followed the orders: G-NH_2 > SDS > u-G (Figure 3b, c, d). The results suggested that (1) G-NH_2 had an ability to produce •OH. (2) SDS had little photochemical activity to generate •OH. (3) u-G had no ability of •OH production.

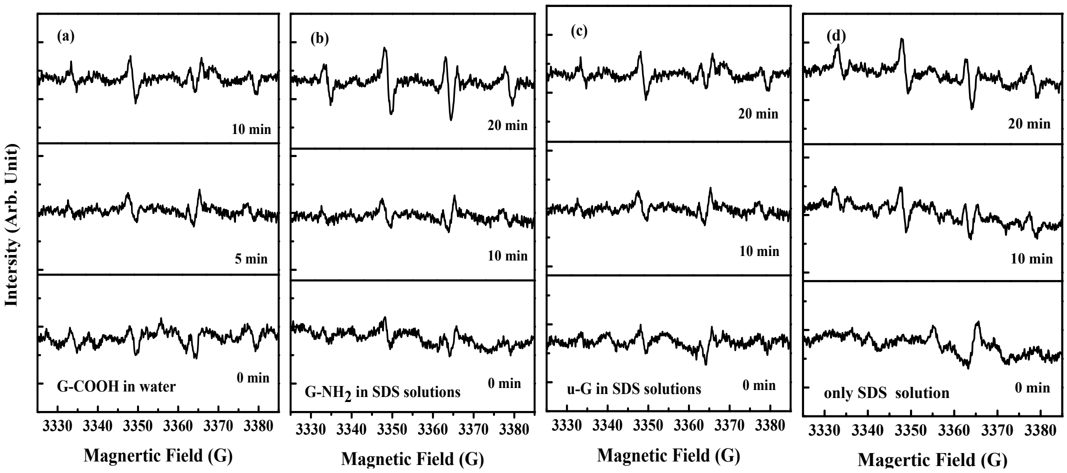

Figure 3. EPR spectrum of DMPO (30 mM) adduct with •OH production in the G-COOH, G-NH_2 and u-G aqueous suspensions (15 mgC/L), and SDS solution (0.05% w/v).

3.3 Kinetics of ROS generation. To quantitatively reveal the production of individual ROS, molecular probe assays were used to determine the photogenerated concentrations of $^1O_2$, •OH and $O_2^{•-}$ in G-COOH, G-NH_2 and u-G aqueous suspensions with or without irradiation. Figure 4a shows the loss concentration of FFA as a function of reaction time in an aqueous suspension of G-COOH, G-NH_2 and u-G. No measurable FFA decay was observed in G-COOH, G-NH_2 and u-G suspensions at the dark conditions, but FFA concentration in both G-COOH and G-NH_2 suspensions decreased significantly with extended irradiation time (0-5 h). The degradation rate of FFA in G-COOH was much greater than that in G-NH_2 during 5 h irradiation, and the pseudo-steady-state concentration of $^1O_2$ ($[^1O_2]_{ss}$) in G-COOH was approximately 2.6 and 2.2 times greater than that in G-NH_2 at 15 and 25 mgC/L, respectively

(Table 1), indicating G-COOH had higher photosensitized capacity for $^1O_2$ production than G-NH_2. This is related to that n→π* transitions of C=O bonds on the surface of G-COOH (Figure 1 b), which contributes to transfer energy to oxygen molecule under the light expose. The $[^1O_2]_{ss}$ induced by 5 mgC/L G-COOH (3.9×10^{-14} M) in this study was roughly 1.2 times higher than previous reported for 5 mg/L SWNTs-COOH (3.3×10^{-14} M) exposed to a UVA-365 nm for 69 h[41]. The result suggested that G-COOH was more likely to transfer energy to produce higher concentrations of $^1O_2$ compared with SWCNTs-COOH, because of the larger specific surface area of graphene layers for light adsorption and O_2 exposure. In this study, the ability of G-NH_2 to photogenerate $^1O_2$ is also reported for the first time. Moreover, it was consistent with our EPR result that no obvious FFA decay was occurred in the u-G suspensions and the SDS solutions (0.05% w/v), which indicated that u-G and SDS had no significant $^1O_2$ production.

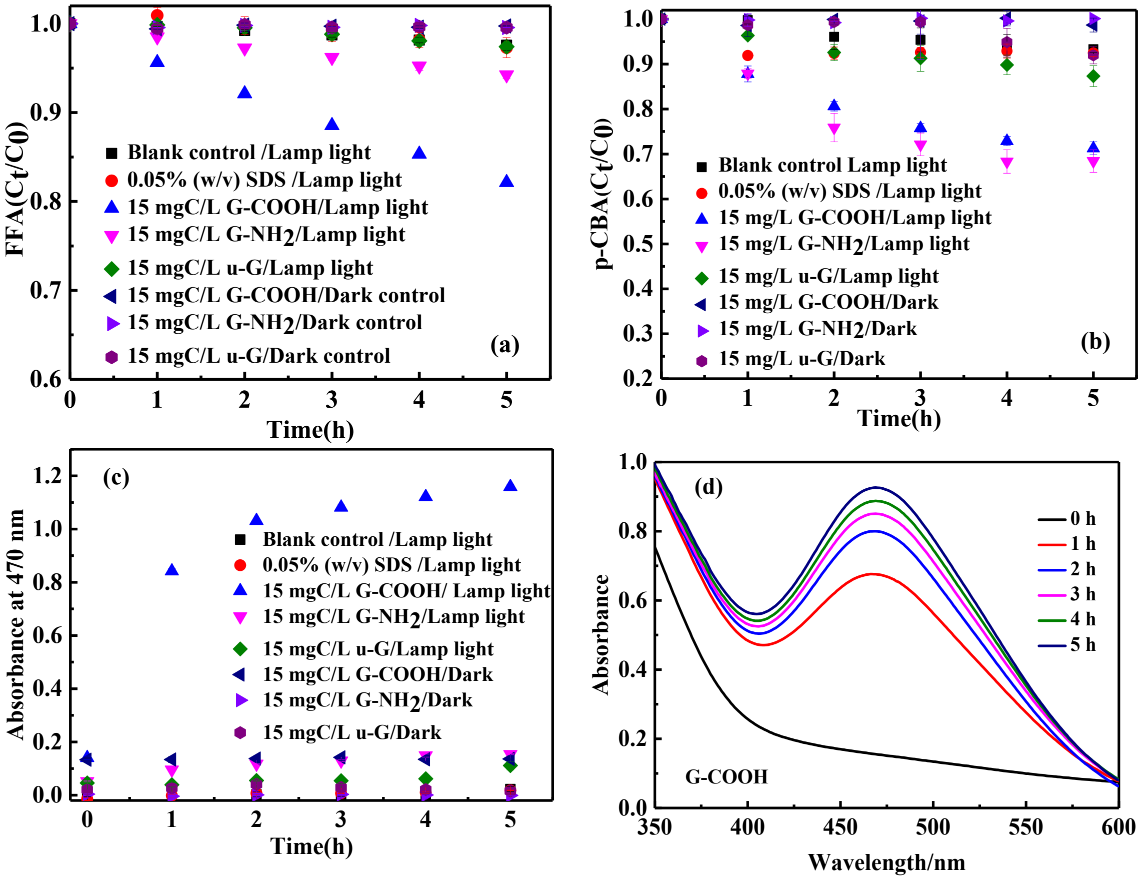

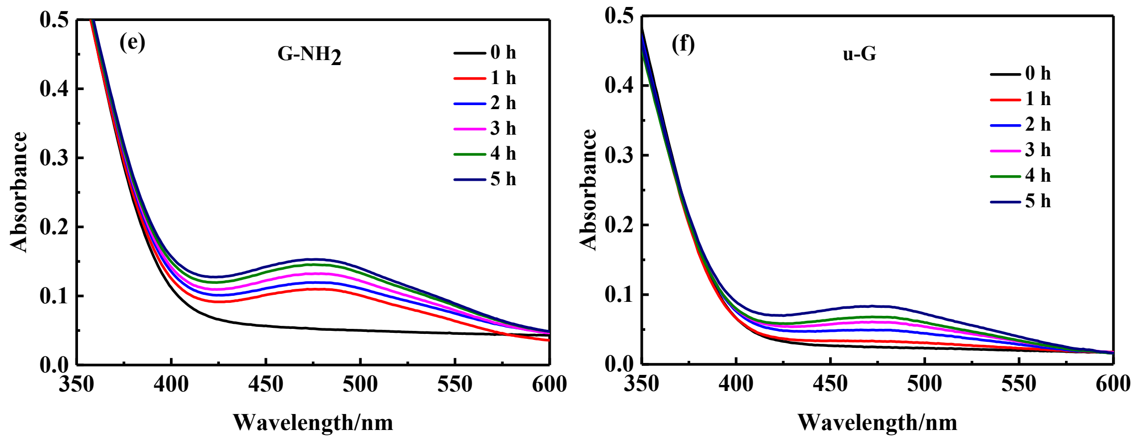

Figure 4. (a) $^1O_2$ generation kinetics indicated by the degradation of 0.2 mM FFA under lamp light, (b) •OH generation kinetics indicated by the degradation of 2 μM *p*-CBA under lamp light, and (c-f) XTT formation indicating $O_2^{\bullet-}$ production by XTT (0.1 mM) under lamp light.

The absorbance of XTT formation was monitored at 470 nm absorption peak in order to quantitatively testing the formation of $O_2^{\bullet-}$. In the dark, there was no significant change on the absorbance at 470 nm in G-COOH, G-NH_2 and u-G suspensions (Figure 4c), which showed no measurable $O_2^{\bullet-}$ production. However, the absorbance of XTT formation increased rapidly in G-COOH suspension during 5 h irradiation (Figure 4d), which indicated that the generation of $O_2^{\bullet-}$ was promoted by irradiation. Meanwhile, the concentration of $O_2^{\bullet-}$ generation followed the decreasing order: G-COOH > G-NH_2 > u-G (Figure 4d, e and f). Besides, it is also worth mentioning that no measurable amount of $O_2^{\bullet-}$ production was detected in SDS (0.05% w/v) (Figure S5), which indicated that the potential impact of SDS on $O_2^{\bullet-}$ generation was negligible for the quantitative detection.

The loss concentration of *p*CBA in an aqueous suspension of G-COOH, G-NH_2 and u-G was determined for indicating •OH production. In the dark, no measurable *p*CBA decay were occurred, but *p*CBA concentration in G-COOH and G-NH_2 decreased significantly 28% and

30% after 5 h irradiation, respectively (Figure 4b), indicating that irradiation had a beneficial effect to •OH production. Moreover, the pseudo-steady-state concentrations of •OH ($[\bullet\mathrm{OH}]_{ss}$) in G-$NH_2$ suspensions was 1.4-fold, 1.2-fold and 1.1-fold more than that in G-COOH at 5, 15 and 25 mgC/L, respectively (Table 1). No obvious *p*CBA decay was occurred in both u-G suspensions and SDS (0.05% w/v), which indicated that u-G and SDS had no significant •OH production.

Carbon nanomaterials i.e., functionalized CNTs and C_{60} were reported to be excited to form the electron-hole pairs through light absorption[14, 19, 41, 43]. The electrons can be transferred to molecular oxygen to $O_2^{\bullet-}$ production and the holes can react with water or hydroxyl ions to form •OH[16, 19, 41]. As reported by previous studies[16, 41], •OH may be produced by the reaction equations (1-2):

$$O_2^{\bullet-} + 2H^+ + e^- \rightarrow H_2O_2 \tag{1}$$

$$H_2O_2 + H^+ + e^- \rightarrow \bullet OH + H_2O \tag{2}$$

The ability of $O_2^{\bullet-}$ and •OH generation depends on the electron-donation capacity of carbon nanomaterials. In order to compare electron-donation capacity of graphene and its surface functionalized derivatives, we determined reduction potential of G-COOH, G-NH_2 and u-G by cyclic voltammetry (Figure S6)[30]. As a results, the reduction potential of G-NH_2, G-COOH and u-G was -0.65, -0.55 and -0.45 V, respectively. Thus, $[\bullet\mathrm{OH}]_{ss}$ by G-COOH and G-NH_2 in decreasing order followed this trend: G-NH_2 > G-COOH. However, the ability of $O_2^{\bullet-}$ generation followed the decreasing order: G-COOH > G-NH_2. It is likely to be that G-COOH shows a significant higher production efficiency of $O_2^{\bullet-}$ than G-NH_2, and $^1O_2$ in solutions tends to produce $O_2^{\bullet-}$[45].

Table 1. Molar Concentrations of ROS Generated and Possible Pathways for Individual ROS Production by the Aqueous Suspensions of G-COOH, G-NH$_2$ and u-G under Irradiation.

Sample	Dose (mg C/L)	$^1O_2$ (×10^{-13} M)	•OH (×10^{-14} M)	Orbital energies calculated by DFT [b]		Possible pathways and Standards (eV) [e]
				E_{LUMO} (eV)	E_{HOMO} (eV)	
G-COOH	5	0.39±0.01	0.11±0.02	-3.60 ~ **-4.28** [c]	-4.44~ -5.12 [c]	$A^* + {}^3O_2 \longrightarrow A + {}^1O_2$ $E_g > 0.97$ [44-46]
	15	1.47±0.02	0.26±0.02			
	25	2.77±0.07	0.41±0.01			
G-NH$_2$	5	N.D. [a]	0.15±0.04	-2.94 ~ **-3.80** [c]	-4.09~ -4.61 [c]	$A^* + O_2 \rightarrow A^{\bullet +} + O_2^{\bullet -}$ $E_{\mathrm{LUMO}} > -4.30$ [47-48]
	15	0.57±0.03	0.31±0.03			
	25	1.26±0.06	0.47±0.09			
u-G	5	N.D. [a]	N.D. [a]	-3.85 (**-4.10** [d])	-4.10 (-4.37 [d])	$A_{ox}^* + H_2O \rightarrow A_{red}^- + \bullet OH$ $E_{\mathrm{HOMO}} < -6.70$ [48-48]
	15	N.D. [a]	N.D. [a]			
	25	N.D. [a]	N.D. [a]			

[a] N.D. means no detectable ROS production. [b] DFT calculation was performed at the B3LYP/3-21G (d,p) level. [c] For G-COOH and G-NH$_2$, the possible 6 configurations were considered in the calculation of frontier molecular orbital energies. The detailed calculation results please see Figure S7 in the supporting information and the range of E_{LUMO} and E_{HOMO} for the 6 configurations is listed in here. [d] The E_{LUMO} (-4.10) and E_{HOMO} (-4.37) values were for graphene with defect (Table S3). [e] A and A* represent carbon nanoparticles and the excited state of carbon nanoparticles, respectively.

3.4 Oxidative stress markers in *Daphnia magna*. E_{LUMO} was determined by the onsets of reduction peaks in cyclic voltammetry curve, which were -4.17, -4.04 and -4.39 eV for G-COOH, G-NH$_2$ and u-G, respectively (Figure S6). Based on the overlaps between biological redox potential (-4.12 to -4.84 eV) and E_{LUMO} of graphene nanomaterial, u-G and G-COOH were predicted to have the potential of inducing oxidative stress. To validate the reliability of the prediction method, we measured the changes of oxidative stress markers (ROS and SOD) in *Daphnia magna* photoinduced by the graphene nanomaterials. As shown in Figure 5a, ROS levels in *Daphnia magna* were significantly increased by G-COOH and u-G during 40 min irradiation. The ROS level in *Daphnia magna* induced by u-G was higher than that induced by G-COOH. However G-NH_2 did not affect the ROS level in *Daphnia magna* during the whole exposure process.

In order to further quantify oxidative stress, SOD activity in *Daphnia magna* were determined. After 20 min irradiation, u-G and G-COOH induced significant increases in SOD activities in *Daphnia magna* (Figure 5b). To avoid oxidative damage caused by excessive ROS induced by u-G and G-COOH, the activity of SOD in *Daphnia magna* increased to eliminate excessive ROS. However, similar to the ROS results, G-NH_2 did not affect the SOD activity in *Daphnia magna* during the whole exposure process, which indicated that G-NH_2 did not cause oxidative stress on *Daphnia magna*. The above experimental results strongly demonstrated that it is reliable to predict the oxidative stress potential at whole animal levels by the overlap of conduction E_{LUMO} levels of graphene nanomaterials with the biological redox potential (-4.12 to -4.84 eV). As far as we know, this is the first attempt to reliably predict the oxidative stress potential for graphene and its surface functionalized derivatives in *Daphnia magna*.

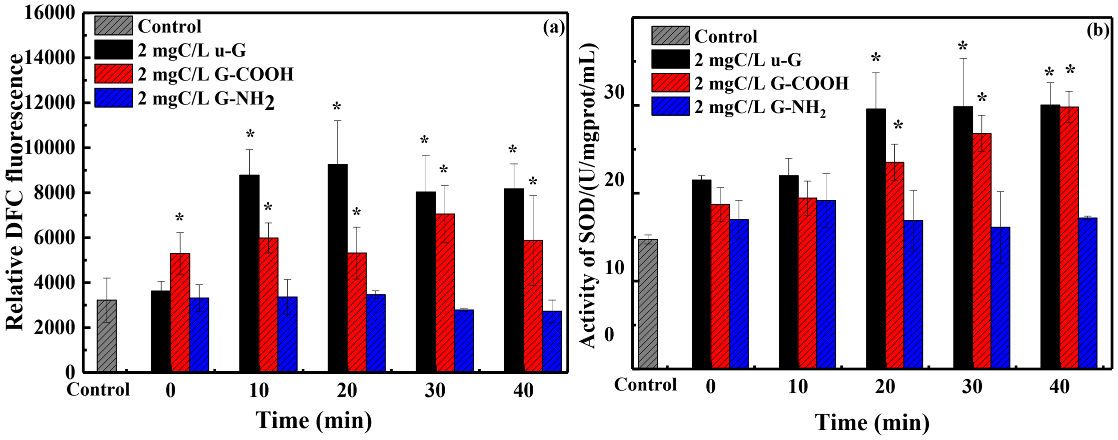

Figure 5. Changes of oxidative stress markers in *Daphnia magna* induced by graphene and its surface functionalized derivatives with different irradiation time ("*" indicates significant differences ($p < 0.05$) between the treatment and the control samples). (a) ROS Level; (b) SOD activity.

3.5 Mechanism for ROS generation. E_{HOMO} and E_{LUMO} of G-COOH and G-NH_2 for six configurations are shown in Figure S7, and the four configurations for u-G with defect are shown in Table S3. By comparing the redox potentials of the individual ROS with the frontier molecular orbital energies of graphene and its functional derivatives, we analyzed the potential reaction pathways of ROS ($^1O_2$, $O_2^{\bullet-}$ and •OH) production.

The lowest E_{LUMO} values calculated by DFT methods for both G-COOH (-4.28 eV) and G-NH_2 (-3.80 eV) are close to the experimental results, suggesting that DFT calculation is adequate for the current study. For u-G, the E_{LUMO} (-3.85 eV) calculated by DFT method was obviously different with experimental value, suggesting the existence of defect on the surface. Considering surface defects, we also tried to calculate E_{LUMO} of u-G with defects, and found that the lowest E_{LUMO} calculated (-4.10 eV, Table S3) are close to the experimental value by cyclic voltammetry.

The generation of $^1O_2$ was driven by photo excitation, the nanoparticles with HOMO-LUMO gap energy (E_g = E_{HOMO}-E_{LUMO}) larger than excitation energy of O_2 (approximately 0.97 eV, Table 1) can be induced to $^1O_2$ generation[44-45]. The calculated E_g of u-G was much less than 0.97 eV. Thus, u-G suspensions could not be photoinduced to produce $^1O_2$. However, the E_g were 1.74, 1.46, 1.22 eV for three configurations of G-COOH, i.e., G-$(COOH)_6$-g3, G-$(COOH)_6$-g4, G-$(COOH)_6$-g6, respectively (Figure S7). And the E_g were 1.31, 1.65, 1.11 eV for three configurations of G-NH_2, i.e., G-$(NH_2)_6$-g3, G-$(NH_2)_6$-g4, G-$(NH_2)_6$-g6, respectively (Figure S7). This indicates that G-COOH and G-NH_2 with one functional group at the *β*-site of zigzag edge (Table S2) could mediate absorbed energy to oxygen and photochemical produced $^1O_2$, which agrees with the experimental observations as shown in Figure 4a. In contrast, the E_g of remaining conformations of G-COOH and G-NH_2 were much less than the excitation energy of O_2 (Figure S7), indicating that they have no ability to photochemical product $^1O_2$.

As shown in Figure 6a, E_{LUMO} of the potential conformations was larger than the redox potentials of $O_2/O_2^{\bullet-}$ (-4.30 eV) for G-COOH, G-NH$_2$ and u-G, implying these nanoparticles could donate electrons to O_2 for the formation of $O_2^{\bullet-}$. It was in good agreement with the experimental results as shown in Figure 4c. Interestingly, the E_{LUMO} values of six configurations for G-COOH were less than the corresponding for G-NH$_2$ (Figure 6a), which is in consistent with our experimental results that the reduction capacity of G-NH$_2$ was larger than G-COOH.

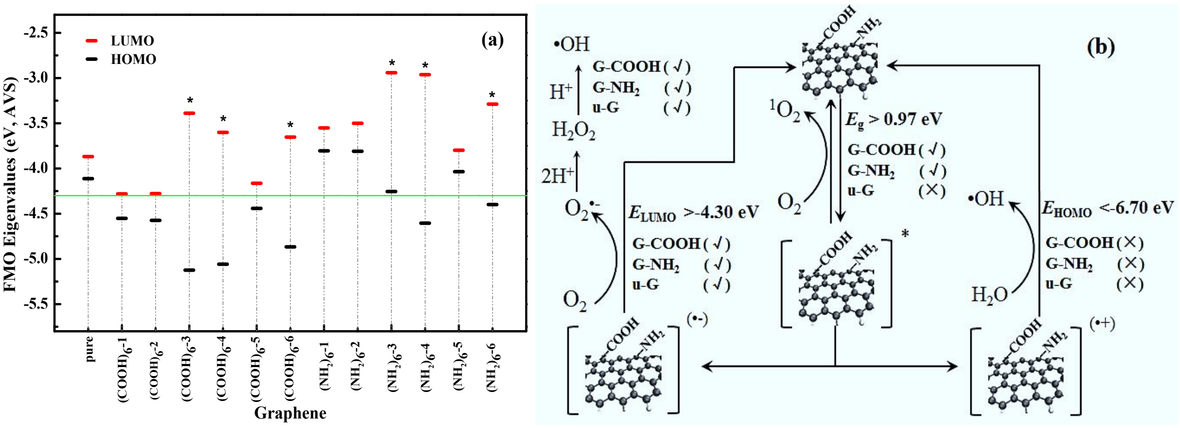

Figure 6. (a) Calculated energy of frontier molecular orbitals (E_{HOMO}, E_{LUMO}) for graphene and their derivatives. (Black and red signs indicate E_{HOMO} and E_{LUMO} levels, respectively. Symbol "*" indicates $^1O_2$ generation of the corresponding conformations. Nanoparticles with E_{LUMO} above green solid line (-4.30 eV) can be considered to induce the formation of $O_2^{\bullet-}$). (b) Proposed reaction mechanism to induce ROS by graphene and their derivatives. ("√" indicates the reaction pathway was occurred, while "×" indicates the reaction pathway was failed.)

The redox potentials for •OH generation was approximately -6.70 eV (Table 1), which was less than the E_{HOMO} values of G-COOH, G-NH$_2$ and u-G. These energy level data indicate that the holes of G-COOH, G-NH$_2$ and u-G are difficult to oxidize H_2O into •OH, which was in accordance with the cyclic voltammetry analysis that G-COOH, G-NH$_2$ and u-G had no oxidation ability in aqueous solution (Figure S6). Thus, the production of •OH was likely only from the reaction equations (1) and (2). Based on DFT calculations, we clarified the possible reaction pathways of ROS generation induced by G-COOH, G-NH_2 and u-G (Figure 6b). G-COOH and G-NH_2 efficiently mediated energy transfer to produce $^1O_2$, G-COOH, G-NH_2 and u-G induced electron transfer to generate $O_2^{\bullet-}$ and further to produce •OH.

4. Overview and conclusion

Graphene could be modified by functional groups through a series of transformation processes after being released into the environment, which greatly influences their potential to produce ROS. To understand the underlying mechanisms of ROS generation induced by graphene and its surface functionalized derivatives, we evaluated the generation kinetics of three types of ROS in aqueous solution under irradiation. The results showed that G-COOH and G-NH_2 efficiently mediated energy transfer to produce $^1O_2$, and the pseudo-steady-state concentration of $^1O_2$ by G-COOH was 2.2~2.6 times higher than G-NH_2 after 5 h irradiation under the same concentration. Meanwhile, G-COOH, G-NH_2 and u-G induced electron transfer to generate $O_2^{\bullet-}$ and further to produce •OH, and the electron-donation capacity followed the decreasing order: G-NH_2 > G-COOH > u-G. These findings strongly suggest that the functionalization of graphene caused by potential biological and chemical transformation or degradation routes under natural conditions, could lead to changes in their photochemical activity that govern their toxicity by ROS generation to aquatic organisms. Based on DFT theory, the frontier molecular orbitals of graphene and its surface functionalized derivatives were calculated. By comparing the ROS generation redox potentials with the frontier molecular orbitals of graphene nanomaterials, we interpreted the ROS generation mechanisms of graphene and its surface functionalized derivatives. The results suggested that (1) G-COOH, G-NH_2 and u-G could donate electrons to O_2 for the formation of $O_2^{\bullet-}$. H_2O_2 was formed by the reaction of $O_2^{\bullet-}$ with H^+ in water. The three graphene nanomaterials could further donate electrons to H_2O_2 for the formation of •OH. (2) G-COOH and G-NH_2 with one functional group at the *β*-site of zigzag edge could mediate absorbed energy to O_2 and photochemical produced $^1O_2$. The calculation results were in good agreement with the experimental results, which strongly suggest that the DFT-based theoretical framework offers an assistance to predict the reaction pathways of ROS production and guide the design of environmentally benign nanomaterials. The oxidative stress potential for graphene nanomaterials were successfully predicted by comparing E_{LUMO} with the levels biological redox potential. The predictive toxicological paradigm is of considerable significance for regulatory decision-making about carbon nanomaterials. Our methodology could be extended beyond graphene to other nanomaterials in future. It has far-reaching implications for sustainable nanotechnology development.

Acknowledgments.

This study was supported in China by the National Natural Science Foundation of China (21477016), the Fundamental Research Funds for the Central Universities (DUT15TD09), and in USA by the National Science Foundation-Centers of Research Excellence in Science and Technology (NSF-CREST Center) for Innovation, Research and Education in Environmental Nanotechnology (CIRE2N) (Grant No. HRD-1736093).

Conflicts of interest.

There are no conflicts of interest to declare.

References

1. Qiu, J.; Geng, H.; Wang, D.; Qian, S.; Zhu, H.; Qiao, Y.; Qian, W.; Liu, X. Layer-number dependent antibacterial and osteogenic behaviors of graphene oxide electrophoretic deposited on Titanium. *ACS Appl. Mater. Inter.* 2017, 9 (14), 12253-12263.
2. Verma, S.; Dutta, R. K. Enhanced ROS generation by ZnO-ammonia modified graphene oxide nanocomposites for photocatalytic degradation of trypan blue dye and 4-nitrophenol. *J. Environ. Chem. Eng.* 2017, 5 (5), 4776-4787.
3. Guo, X.; Dong, S.; Petersen, E. J.; Gao, S.; Huang, Q.; Mao, L. Biological uptake and depuration of radio-labeled graphene by Daphnia magna. *Environ. Sci. Technol.* 2013, 47 (21), 12524-12531.
4. Dong, S.; Xia, T.; Yang, Y.; Lin, S.; Mao, L. Bioaccumulation of 14C-Labeled graphene in an aquatic food chain through direct uptake or trophic transfer. *Environ. Sci. Technol.* 2018, 52 (2), 541-549.
5. Ou, L.; Song, B.; Liang, H.; Liu, J.; Feng, X.; Deng, B.; Sun, T.; Shao, L. Toxicity of graphene-family nanoparticles: a general review of the origins and mechanisms. *Part. Fibre. Toxicol.* 2016, 13 (1), 57.
6. Sutherland, M. W.; Learmonth, B. A. The tetrazolium dyes MTS and XTT provide new quantitative assays for superoxide and superoxide dismutase. *Free. Radic. Res. Comm.* 1997, 27 (3), 283-289.
7. Chiste, R. C.; Freitas, M.; Mercadante. A. Z.; Fernandes, E. Superoxide anion radical: generation and detection in cellular and non-cellular systems. *Curr. Med. Chem.* 2015, 22 (37), 4234-4256.
8. Suh,Y. A.; Arnold, R. S.; Lassegue, B.; Shi, J.; Xu, X. X.; Sorescu, D.; Chung, A. B.; Griendling, K. K.; Lambeth, J. D. Cell transformation by the superoxide-generating oxidase Mox1. *Nature.* 1999, 401 (6748), 79-82.
9. Luo, T.; Chen, J.; Song, B.; Ma, H.; Fu, Z.; Peijnenburg, W. J. G. M. Time-gated luminescence imaging of singlet oxygen photoinduced by fluoroquinolones and functionalized graphenes in *Daphnia magna*. *Aquat. Toxicol.* 2017, 191, 105-112.
10. Zhang, X.; Zhou, Q.; Zou, W.; Hu, X. Molecular mechanisms of developmental toxicity induced by graphene oxide at predicted environmental concentrations. *Environ. Sci. Technol.* 2017, 51 (14), 7861-7871.
11. Hu, X.; Zhou, M.; Zhou, Q. Ambient water and visible-light irradiation drive changes in graphene morphology, structure, surface chemistry, aggregation, and toxicity. *Environ. Sci. Technol.* 2015, 49 (6), 3410-3418.
12. Kong, L.; Zepp, R. G. Production and consumption of reactive oxygen species by fullerenes. *Environ. Toxicol. Chem.* 2011, 31 (1), 136-143.
13. Chen, C. Y.; Jafvert, C. T. The role of surface functionalization in the solar light-induced production of reactive oxygen species by single-walled carbon nanotubes in water. *Carbon.* 2011, 49 (15), 5099-5106.
14. Zhao, Y.; Jafvert, C. T. Environmental photochemistry of single layered graphene oxide in water. Environ. Sci-Nano. 2015, 2 (2), 136-142.
15. Toxicity Testing in the 21st Century: A Vision and a Strategy; National Research Council. 2007.

16. Environmental, Health, and Safety Research Strategy; National Science and Technology Council. 2011.

17. Li, Y.; Zhang, W.; Niu, J.; Chen, Y. Mechanism of photogenerated reactive oxygen species and correlation with the antibacterial properties of engineered metal-oxide nanoparticles. *ACS Nano.* 2012, 6 (6), 5164-5173.

18. Wang, Dan; Zhao, L; Ma, H; Zhang, H; Guo, L. Quantitative Analysis of Reactive Oxygen Species Photogenerated on Metal Oxide Nanoparticles and Their Bacteria Toxicity: The Role of Superoxide Radicals. Environl. Sci. Technol. 2017, 51(17):10137-10145.

19. Zhang, H.; Ji, Z.; Xia, T.; Meng, H.; Lowkam, C.; Liu, R.; Pokhrel, S.; Lin, S.; Wang, X.; Liao, Y. P. Use of metal oxide nanoparticle band gap to develop a predictive paradigm for oxidative stress and acute pulmonary inflammation. *ACS Nano.* 2012, 6 (5), 4349-4368.

20. Ge, L.; Chen, J.; Qiao, X.; Lin, J.; Cai, X. Light-source-dependent effects of main water constituents on photodegradation of phenicol antibiotics: mechanism and kinetics. *Environl. Sci. Technol.* 2009, 43 (9), 3101-3107.

21. Lee, J.; Yamakoshi, Y.; Hughes, J. B.; Kim, J. H. Mechanism of C_{60} photoreactivity in water: fate of triplet State and radical anion and production of reactive oxygen species. *Environl. Sci. Technol.* 2008, 42 (9), 3459-64.

22. Haag, W. R.; Hoigne, J. Singlet oxygen in surface waters. 3. Photochemical formation and steady-state concentrations in various types of waters. *Environl. Sci. Technol.* 1986, 20 (4), 341-348.

23. Elovitz, M. S.; Gunten, U. V.; Kaiser, H. P. Hydroxyl radical/Ozone ratios during ozonation processes. II. The effect of temperature, pH, Alkalinity, and DOM Properties. *Ozone. Sci. Eng.* 2000, 22 (2), 123-150.

24. Martin, U.; Andreas, S.; Birgit Roth, Z.; Alexander, S.; Christa, B.; Buehler, K. P.; Ludwig, L.; Corinne, C.; Stark, W. J.; Beatrice, B. S. Inflammatory response of lung macrophages and epithelial cells after exposure to redox active nanoparticles: effect of solubility and antioxidant treatment. *Environl. Sci. Technol.* 2014, 48 (23), 13960- 13968.

25. Luo, T.; Chen, J.; Li, X.; Zhang, S.; Yao, H.; Peijnenburg, W. J. G. M. Effects of lomefloxacin on survival, growth and reproduction of *Daphnia magna* under simulated sunlight radiation. *Ecotox. Environ. Safe*. 2018, 166, 63-70.

26. Casolo, S.; Løvvik, O. M.; Martinazzo, R.; Tantardini, G. F. Understanding adsorption of hydrogen atoms on graphene. *J. Chem. Phys.* 2009, 130 (5).

27. Lone, B.; Scheiner, S.; Kar, T. Competition between carboxylic and phenolic groups for the preferred sites at the periphery of graphene-A DFT study. *Carbon.* 2014, 80 (1), 405-418.

28. Yuge, R.; Zhang, M.; Tomonari, M.; Yoshitake, T.; Iijima, S.; Yudasaka, M. Site identification of carboxyl groups on graphene edges with Pt derivatives. *ACS Nano.* 2008, 2 (9), 1865-1870.

29. Kar, T.; Scheiner, S.; Adhikari, U.; Roy, A. K. Site preferences of carboyxl groups on the periphery of graphene and their characteristic IR spectra. *J. Phys. Chem. C.* 2012, 117, (35) 18206-18215.

30. Liu, J.; Li, B. W.; Tan, Y. Z.; Giannakopoulos, A.; Sanchezsanchez, C.; Beljonne, D.;

Ruffieux, P.; Fasel, R.; Feng, X.; Müllen, K. Toward cove-edged low band gap graphene nanoribbons. *J. Am. Chem. Soc.* 2015, 137 (18), 6097-103.

31. Beheshtian, J.; Peyghan, A. A. Functionalization of BN nanosheet with N2H4 may be feasible in the presence of Stone-Wales defect. *Struct. Chem.* 2013, 24 (5), 1565-1570.
32. Frisch, M. J.; Trucks, G. W.; Schlegel, H, B. Gaussian, Inc, Wallingford CT, 2009.
33. Robles, J.; López, M. J.; Alonso, J. A. Modeling of the functionalization of single-wall carbon nanotubes towards its solubilization in an aqueous medium. *Eur. Phys. J. D.* 2011, 61 (2), 381-388.
34. Kudin, K. N.; Ozbas, B.; Schniepp, H. C.; Prud'homme, R. K.; A, I. Raman spectra of graphite oxide and functionalized graphene sheets. *Nano. Lett.* 2008, 8 (1), 36-41.
35. Fasolino, A.; Los, J. H.; Katsnelson, M. I. Intrinsic ripples in graphene. *Nature. Mater.* 2007, 6 (11), 858-861.
36. Matsumoto, Y.; Koinuma, M.; Ida, S.; Hayami, S.; Taniguchi, T.; Hatakeyama, K.; Tateishi, H.; Watanabe, Y.; Amano, S. Photoreaction of Graphene Oxide Nanosheets in Water. *J. Phys. Chem. C.* 2011, 115 (39), 19280-19286.
37. Hou, W. C.; Chowdhury, I.; Jr, G. D.; Henderson, W. M.; Fairbrother, D. H.; Bouchard, D.; Zepp, R. G. Photochemical transformation of graphene oxide in sunlight. *Environ. Sci. Technol.* 2015, 49 (6), 3435-43.
38. Qu, X.; Alvarez, P. J.; Li, Q. Photochemical transformation of carboxylated multiwalled carbon nanotubes: role of reactive oxygen species. *Environ. Sci. Technol.* 2013, 47 (24), 14080-14088.
39. Chen, D.; Li, L.; Guo, L. An environment-friendly preparation of reduced graphene oxide nanosheets via amino acid. *Nanotechnology*. 2011, 22 (32), 325601.
40. Wang, C.; Zhou, G.; Liu, H.; Wu, J.; Qiu, Y.; Gu, B. L.; Duan, W. Chemical functionalization of carbon nanotubes by carboxyl groups on stone-wales defects: a density functional theory study. *J. Phys. Chem. B.* 2006, 110 (21), 10266.
41. Wang, X.; Qu, R.; Huang, Q.; Wei, Z.; Wang, Z. Hepatic oxidative stress and catalyst metals accumulation in goldfish exposed to carbon nanotubes under different pH levels. *Aquat. Toxicol.* 2015, 160, 142-150.
42. Gu, C.; Wang, J.; Guo, M.; Sui, M.; Lu, H.; Liu, G. Extracellular degradation of tetrabromobisphenol A via biogenic reactive oxygen species by a marine *Pseudoalteromonas sp. Water. Res.* 2018, 142, 354-362.
43. Kim, F.; Cote, L. J.; Huang, J. Graphene oxide: surface activity and two-dimensional assembly. *Adv. Mater.* 2010, 22 (17), 1954-1958.
44. Maurette, M.; Oliveros, E.; Infelta, P. P.; Ramsteiner, K.; Braun, A. M. Singlet oxygen and superoxide: experimental differentiation and analysis. *Helv. Chim. Acta.* 2010, 66 (2), 722-733.
45. Hou, W. C.; Jafvert, C. T. Photochemistry of aqueous C_{60} clusters: evidence of $^1O_2$ formation and its role in mediating C_{60} phototransformation. *Environ. Sci. Technol.* 2009, 43 (14), 5257-5262.
46. Schweitzer, C.; Schmidt, R. Physical mechanisms of generation and deactivation of singlet oxygen. *Chem. Rev.* 2003, 34 (29), 1685-1757.
47. Li, Y.; Zhang, W.; Niu, J.; Chen, Y. Mechanism of photogenerated reactive oxygen species and correlation with the antibacterial properties of engineered metal-oxide

nanoparticles. *ACS Nano.* 2012, 6 (6), 5164-5173.

48. Burello, E.; Worth, A. P. A theoretical framework for predicting the oxidative stress potential of oxide nanoparticles. *Nanotoxicology.* 2011, 5 (2), 228-235.

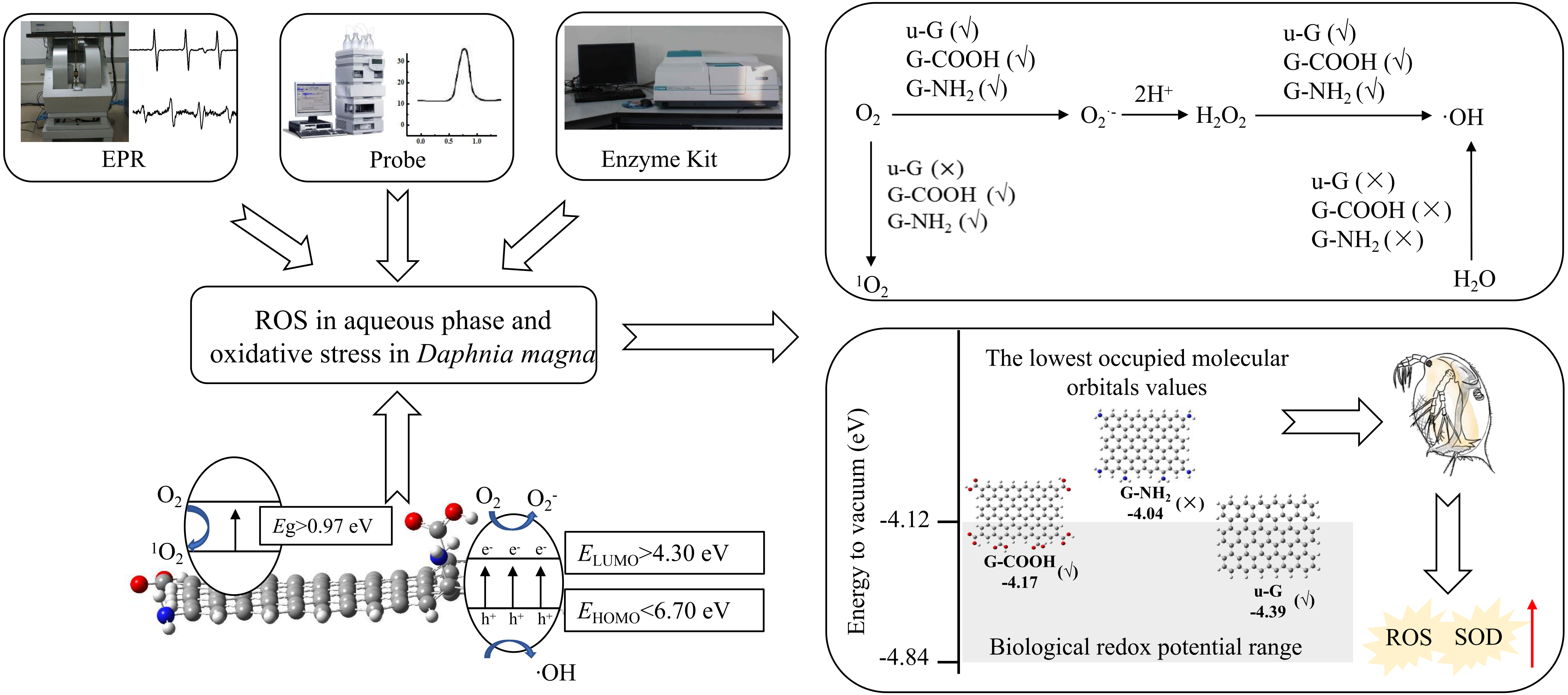
EPR
Probe
Enzyme Kit
ROS in aqueous phase and oxidative stress in *Daphnia magna*
O_2
$^1O_2$
*E*g>0.97 eV
O_2
O_2^-
e- e- e-
h+ h+ h+
E_{LUMO}>4.30 eV
E_{HOMO}<6.70 eV
·OH
u-G (√)
G-COOH (√)
$G-NH_2$ (√)
O_2
$O_2^{\cdot -}$
$2H^+$
H_2O_2
u-G (√)
G-COOH (√)
$G-NH_2$ (√)
·OH
u-G (×)
G-COOH (√)
$G-NH_2$ (√)
$^1O_2$
u-G (×)
G-COOH (×)
$G-NH_2$ (×)
H_2O
Energy to vacuum (eV)
-4.12
-4.84
The lowest occupied molecular orbitals values
$G-NH_2$ (×)
-4.04
G-COOH (√)
-4.17
u-G (√)
-4.39
Biological redox potential range
ROS
SOD